Combustion and Flame 256 (2023) 112994

Contents lists available at ScienceDirect

Combustion and Flame

journal homepage: www.elsevier.com/locate/combustflame

Combustion studies of MMA/GO_x for a hybrid rocket motor

Chandru Dhandapani[a,1,*], Guillaume Blanquart[a], Ashley C. Karp[b], Elizabeth T. Jens[b], Jason Rabinovitch[c]

[a] California Institute of Technology, Pasadena, CA 91125, United States
[b] Jet Propulsion Laboratory, California Institute of Technology, Pasadena, CA 91109, United States
[c] Stevens Institute of Technology, Hoboken, NJ 07030, United States

ARTICLE INFO

Article history:
Received 8 December 2021
Revised 26 July 2023
Accepted 27 July 2023

Keywords:
Computational Fluid Dynamics
Hybrid rockets
Turbulent flames
MMA
Diffusion flames

ABSTRACT

Poly(methyl methacrylate) (PMMA) is the synthetic polymer of methyl methacrylate (MMA), which is used in a multitude of everyday applications, can also be used as a solid fuel in hybrid rockets. When used as a fuel in a combustion chamber, PMMA undergoes thermal decomposition and phase-change (solid-to-gas), where gaseous MMA ($C_5H_8O_2$) is the primary product. The gaseous MMA then undergoes combustion with an oxidizer. Experimental studies of this combustion chamber have been performed in literature, and this study helps produce high-fidelity simulations, which can match experimental observations while giving access to more data in the combustion chamber. Simulations of turbulent diffusion flames are performed with gaseous MMA introduced through the combustion chamber walls. Two different diffusion models are used alongside a finite-rate chemistry model to observe the effects of differential diffusion. The rate of inflow of MMA is controlled by the temperature field in the combustion chamber, and the results from the 3D simulation are comparable to 1D counterflow diffusion flame simulations. Simulations are also performed with a tabulated chemistry model developed to improve the computational efficiency and with two different internal diameters to analyze the geometric effects. If one wishes to capture the flow field profiles and fuel regression rate, chemistry effects need to be included. If one wishes to capture the internal chemistry profiles of the combustion products, differential diffusion effects are important. The fuel regression rate and the radial chemistry profiles from the simulations are compared with the experimental results and show good agreement.

1. Introduction

Hybrid rocket motors are chemical propulsion systems that use fuel and oxidizer stored in different phases. Typically, a solid fuel grain is used with a liquid or gaseous oxidizer, as shown in Fig. 1. The inert fuel grain is stored in the combustion chamber and the oxidizer is stored in a pressurized tank. The oxidizer is introduced to the combustion chamber through the main control valve which can be used to throttle or stop combustion by controlling the oxidizer mass flow rate. Most propellant combinations for hybrid rocket motors are not hypergolic, so an igniter is used to provide the activation energy to commence combustion [1,2]. Combustion primarily occurs within a boundary layer above the surface of the fuel, and if present, also within a post-combustion chamber. Combustion products are exhausted through a converging-diverging nozzle to generate thrust.

Hybrid rockets are promising for a number of applications depending on the propellants. The propellant combination discussed here is PMMA/Gaseous oxygen (GO_x). Poly(methyl methacrylate) (PMMA) is the synthetic polymer of methyl methacrylate (MMA), commonly known as acrylic. When heated, solid PMMA undergoes thermal decomposition and phase-change into predominantly gaseous MMA ($C_5H_8O_2$), which then undergoes oxidation into carbon dioxide (CO_2), water (H_2O), carbon monoxide (CO), and low-molecular-weight compounds, including formaldehyde (CH_2O).

PMMA has been researched as a hybrid rocket fuel since the initial concept of hybrid rocket motors was developed [3]. It continues to be used as a representative classical hybrid rocket fuel in various combustion experiments [4–7], and has also been researched as a fuel for solid fuel ramjets (SFRJs) [8,9].

Previous experimental research efforts on hybrid motor combustion with PMMA and GO_x were used to assess the feasibility of using this propellant combination in small spacecraft [2,10–12]. These tests focused on evaluating fuel regression rate at various chamber pressures as well as a demonstration of the ignition system in a low-pressure environment.

* Corresponding author.
E-mail address: chandru.dhandapani@pnnl.gov (C. Dhandapani).
[1] 1055, E Union St, Apt 4, Pasadena, CA 91106.

https://doi.org/10.1016/j.combustflame.2023.112994
0010-2180/

More recently, Mechentel et al. designed an experimental setup, representative of these hybrid rocket motors [13,14]. The combustion chamber consists of the oxidizer (O_2) flowing through a cylindrical port, with the walls made of solid PMMA. Experiments were conducted to observe the impact of several parameters (including chamber pressure and burn time) on the burner behavior and fuel regression rate.

Finally, Bendana et al. designed a facility to visualize and quantify hybrid combustion in situ using Laser Spectroscopy [15]. The facility has the capability to measure temperature and the mole fractions of CO, H_2O, and CO_2 along the length of the fuel grain. This is done by taking measurements at the outlet of multiple fuel grains (of varying length) and interpolating between them. The measurements to date have all been performed at atmospheric combustion chamber pressure, without a converging-diverging nozzle.

These experimental tests are expensive to perform and quite complicated to set up. They can be used to observe the global behavior and measure quantities of interest (QOIs) such as regression rate and regression profile, but the complex chemistry of these reacting flows and its interaction with the fluid mechanics can only be observed using simulations. Numerical simulations provide the full velocity field, chemical composition, and thermodynamic properties throughout the domain, from which the relevant quantities of interest may be computed, without the high amount of resources needed by experiments. However, numerical simulation results must be validated with relevant experimental data.

Numerical simulations of hybrid rocket motors have been performed in the past, but most used different solid fuels such as Polyethylene [16] and Hydroxyl-Terminated Poly-Butadiene (HTPB) [17]. Simulations with HTPB as fuel were performed using a reduced combustion model for 1,3-butadiene combustion consisting of 9 species and 6 reactions [17,18], though it is acknowledged that the decomposition of HTPB is quite complex and not captured in current modeling studies [19,20].

Numerical studies of PMMA, however, have only been performed for pyrolysis of PMMA under laminar conditions [21,22] or with Reynolds-averaging [23]. Recently, a combustion model for $C_5H_8O_2$ and GO_x was developed, which consists of 88 species and 1084 elementary reactions [24]. This high numerical complexity results in increased computational costs and simulations of rocket motors can be prohibitively expensive.

Hybrid rocket combustors present rich fluid mechanics phenomena including high speed shear layers, low speed recirculation regions, stagnation points, turbulent wall bounded flows, and wall normal mass injection. Similar challenges exist on the combustion side with solid to gaseous fuel conversion, heavy hydrocarbon chemistry, and coupled heat transfer-mass injection. In this context, the objectives of the present work are four-folds. Acknowledging that a full Direct Numerical Simulation (DNS) would be computationally prohibitive, the first objective is to assess if a hybrid DNS-LES approach can be used successfully to simulate the overall reacting flow field. The second objective is to observe the effects of differential diffusion in these reacting flow simulations. The third objective is to analyze the structure of the ensuing diffusion flame using detailed chemistry and to extract from it a reduced order model. The fourth and final objective is to perform an in-depth comparison with experimental data focusing not only on global quantities, but also on local radial profiles.

The target experiment for comparison with the current study is that of the combustion chamber used by Bendana et al. [15], which offers a unique opportunity for numerical study. The experiment was performed at atmospheric pressure, using a relatively low mass flow rate of gaseous oxygen, which helps reduce the numerical cost of the simulations, due to the lower turbulence levels. In addition, the laser measurements offer an opportunity for quantitative comparison of species profiles, in addition to global quantities such as average regression rate.

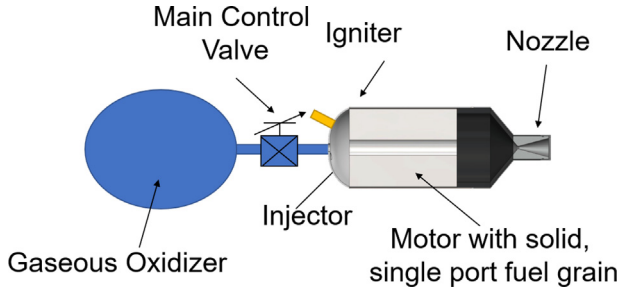

Fig. 1. General schematic of a hybrid rocket motor.

The goal of the study is to simulate these turbulent flames in the combustion chamber and to compare QOIs between the numerical and experimental results. The solid fuel regression and the subsequent non-uniform fuel injection at the combustion chamber wall needs to be modeled appropriately. From these simulations, QOIs such as regression rate profile, heat flux profile, thermal efficiency, chemical composition, etc. can be estimated. The objective of this work is to perform these simulations and quantify discrepancies with the experimental results. If an adequate agreement is shown, then these simulations can be used as predictive methods that can complement experiments and provide optimized operating parameters for full-scale tests of hybrid rocket motors.

The computational framework, including the governing equations, the geometry, boundary conditions, and the simulation configurations, is presented in Section 2. The results are discussed in Section 3. Finally, concluding remarks are presented in Section 4.

2. Computational framework

2.1. Governing equations

The simulations are performed using NGA [25], a finite difference solver with an energy-conserving scheme on a staggered grid, designed to simulate variable-density low Mach number turbulent flows. The scheme is second-order accurate in space, and a semi-implicit second-order Crank-Nicolson scheme is used for time integration [26]. The scalar transport scheme chosen is the third order BQUICK [27] scheme, which ensures that scalars stay within bounds. The governing equations used in NGA under the low Mach number assumption are given below.

The conservation of mass is given by

$$\frac{\partial \rho}{\partial t} + \nabla \cdot (\rho \boldsymbol{u}) = 0, \tag{1}$$

where ρ is the density, and $\boldsymbol{u} = \{u, v, w\}$ is the velocity field. The linear momentum equation is

$$\frac{\partial}{\partial t}(\rho \boldsymbol{u}) + \nabla \cdot (\rho \boldsymbol{u} \otimes \boldsymbol{u}) = -\nabla p + \nabla \cdot \underline{\underline{\boldsymbol{\tau}}}, \tag{2}$$

where p is the hydrodynamic pressure field, and $\underline{\underline{\boldsymbol{\tau}}}$ is the viscous stress tensor, given by

$$\underline{\underline{\boldsymbol{\tau}}} = (\mu + \mu_T)\left(\underline{\underline{\nabla \boldsymbol{u}}} + (\underline{\underline{\nabla \boldsymbol{u}}})^T\right) - \frac{2}{3}(\mu + \mu_T)(\nabla \cdot \boldsymbol{u})\underline{\underline{\boldsymbol{I}}}, \tag{3}$$

where $\underline{\underline{\boldsymbol{I}}}$ is the identity tensor, μ is the dynamic viscosity of the mixture, and μ_T is the subfilter scale viscosity. The viscosity is calculated from the composition of the mixture using a modified version of Wilke's formula [28], and the individual species viscosities are obtained using standard kinetic theory [29]. The species transport equation is expressed as

$$\frac{\partial}{\partial t}(\rho Y_i) + \nabla \cdot (\rho \boldsymbol{u} Y_i) = -\nabla \cdot \boldsymbol{j}_i + \dot{\omega}_i, \tag{4}$$

where Y_i, $\dot{\omega}_i$, and $\boldsymbol{j}_i$ are the mass fraction, production rate, and diffusion flux, respectively, of species i. The diffusion flux is calculated as

$$\boldsymbol{j}_i = -\rho\left(D_{i,m} + D_{i,T}\right)\frac{Y_i}{X_i}\nabla X_i + \rho Y_i \boldsymbol{u}_c, \tag{5}$$

where $D_{i,m}$ is the ith species mixture-averaged diffusion coefficient [30,31] and $D_{i,T}$ is the sub-filter scale diffusivity. X_i is the species mole fraction, and $\boldsymbol{u}_c$ is a correction velocity calculated to ensure that the net diffusion mass flux, $\Sigma_i \boldsymbol{j}_i$ is zero [32,33].

In the present study, two different methods are used to model diffusion in the simulations using detailed chemistry. The first method, henceforth called the mixture-averaged (MA) case, uses the mixture-averaged diffusion model. In the second detailed chemistry simulation, the species Lewis numbers are assumed to be unity, $\mathrm{Le}_i = \alpha/D_i = 1$, where $\alpha = \lambda/(\rho c_p)$ is the thermal diffusivity of the mixture. λ is the thermal conductivity of the mixture and is calculated from the composition of the mixture and the individual values [34]. The individual species thermal conductivities are calculated using a modified version of Eucken's formula [35]. The conservation of specific enthalpy and specific internal energy is used to derive a transport equation for temperature, T, under the low Mach number approximation. This transport equation is given by

$$\frac{\partial}{\partial t}(\rho T) + \nabla\cdot(\rho \boldsymbol{u} T) = \nabla\cdot(\rho\alpha\nabla T) + \dot{\omega}_T - \frac{1}{c_p}\sum_i c_{p,i}\boldsymbol{j}_i\cdot\nabla T + \frac{\rho\alpha}{c_p}\nabla c_p\cdot\nabla T, \tag{6}$$

where $c_{p,i}$ is the heat capacity of species i, $c_p = \sum_i Y_i c_{p,i}$ is the heat capacity of the mixture, and $\dot{\omega}_T = -1/c_p \sum_i h_i \dot{\omega}_i$ is the temperature source term, where h_i is the specific enthalpy of species, i. The other two terms on the right hand side correspond to heat transfer by conduction and the enthalpy flux term due to molecular diffusion. Heat transfer by radiation is assumed to have little effect on the flow and excluded from the current simulations. The equation of state used to bring closure to this system of equations is given by

$$P_0 = \rho R T \sum_i \frac{Y_i}{W_i} \tag{7}$$

where P_0 is the thermodynamic pressure, R is the universal gas constant, and W_i is the molecular weight of species i. Using the low Mach number assumption, the fluctuations in the hydrodynamic pressure field, p, are small compared to the constant thermodynamic pressure, P_0, used in the equation of state. The thermodynamic pressure is chosen to be 1 atm for all the simulations in this study.

These equations are solved to obtain the unknown variables - $(\rho, u, v, w, T, Y_i, p, W)$. The hydrodynamic pressure field is calculated using a Poisson solver, to satisfy the conservation of mass. The simulations employ the MMA reaction mechanism by Dakshinamurthy et al., which consists of 88 species and 1084 reactions [24].

While the grid resolution (discussed in the following section) is sufficient to resolve all the flow features in the combustion chamber, it may not be sufficient in certain regions of the shear layer when the oxidizer initially enters the chamber. That is why a dynamic Smagorinsky subgrid-scale model is used [36,37]. The model calculates a turbulent viscosity, μ_T, and adds it to the molecular viscosity, μ, in the linear momentum equation and adds similar turbulent diffusivities, $D_{i,T}$, in the species transport equations.

2.2. Geometry details

The computational domain for the turbulent simulations is chosen to match that of the experimental setup by Bendana et al. [15] (see Fig. 2). The combustion chamber has a diameter of 12.7 mm (0.5 in.) and a length of $L_p = 139.7$ mm (5.5 in). The pre-combustion chamber has a diameter of 17.78 mm (0.7 in.) and a length of 15.24 mm (0.6 in.), with an inflow through an injector of 5.08 mm (0.2 in.) diameter. The grid spacing is uniform in the axial direction (250 μm), and a stretched grid spacing is used in the radial direction, with a refined grid near the walls (10 μm at the wall). The computational grid is cylindrical with $619 \times 186 \times 128 = 14.7$ million grid points, with approximately 11.6 million of those grid points representing points in the flowfield, and the rest representing grid points in the walls which are not used in the calculations.

Experiments were performed using different lengths of fuel grains at 12.7 mm (0.5 in.) intervals, with a minimum fuel grain length of 25.4 mm (1 in.), and a maximum length of 139.7 mm (5.5 in.). The hollow port through these fuel grains works as the combustion chamber, with the fuel grain working as its walls, then surrounded by ambient air. The experimental results were obtained from Laser-Aided Tomography (LAT) measurements 0.5 mm downstream of the exit plane of the different fuel grains, allowing the experimental measurements to extend beyond the internal radius of 6.35 mm = 0.25 in, as they are not restricted by the walls of the combustion chamber.

As observed in the experimental results, the regression rate of the solid fuel is about $0.08 - 0.12$ mm/s. With a burn time of the experiments of around $8 - 10\,s$, the internal radius of the fuel port can increase by about 1 mm. To investigate the effects of this fuel regression, two sets of simulations are performed. The first set of simulations uses the initial internal radius of the combustion chamber, i.e. 6.35 mm (= 0.25 in.). The second set is performed with a larger radius. Specifically, the internal radius of the combustion chamber is chosen to be 6.858 mm (= 0.27 in), which would be the internal radius around $4 - 5\,s$ through the burn, when the experimental measurements are made. Other details including the injector and pre-combustion chamber diameter and the mass flow rate are kept the same in the large diameter simulations.

2.3. Oxygen inlet

The injector velocity field (i.e. oxygen inlet for the full computational domain) for the combustion simulations is obtained by performing two sequential Large Eddy Simulations (LES). The mass rate of oxygen is $1.2 g/s$ and the temperature is $298 K$.

The first simulation is that of a turbulent pipe flow in a cylindrical domain of length 25.4 mm (1 in.) and an internal diameter of 5.08 mm (0.2 in), with periodic boundary conditions in the axial direction. This simulates the fully developed turbulent flow seen in the injector pipe. The cylindrical domain had a grid resolution of $192 \times 72 \times 96$, with uniform grid spacing in the axial (192) and azimuthal (96) directions and with quadratic grid stretching in the radial direction, starting with a grid spacing of 5.3 microns near the wall. The instantaneous axial velocity contours are plotted in Fig. 3(a).

The velocity information from the exit plane is used as the inlet for the second simulations, for which the pipe diameter is not constant and includes a wider expansion chamber of length 17.02 mm (0.67 in.) and an internal diameter of 6.35 mm (0.25 in.). This geometry matches the injector geometry in the experimental setup of Bendana et al. seen in Fig. 2 [15]. The cylindrical domain had a grid resolution of $288 \times 94 \times 96$, with uniform grid spacing in the axial (288) and azimuthal (96) directions. The radial resolution from the axis to the injector diameter (first 72 grid points) is the same as that of the previous simulation, with additional quadratic grid stretching in the radial direction implemented in the region between the injector diameter and the expansion chamber diameter (22 grid points). The instantaneous axial velocity contours are

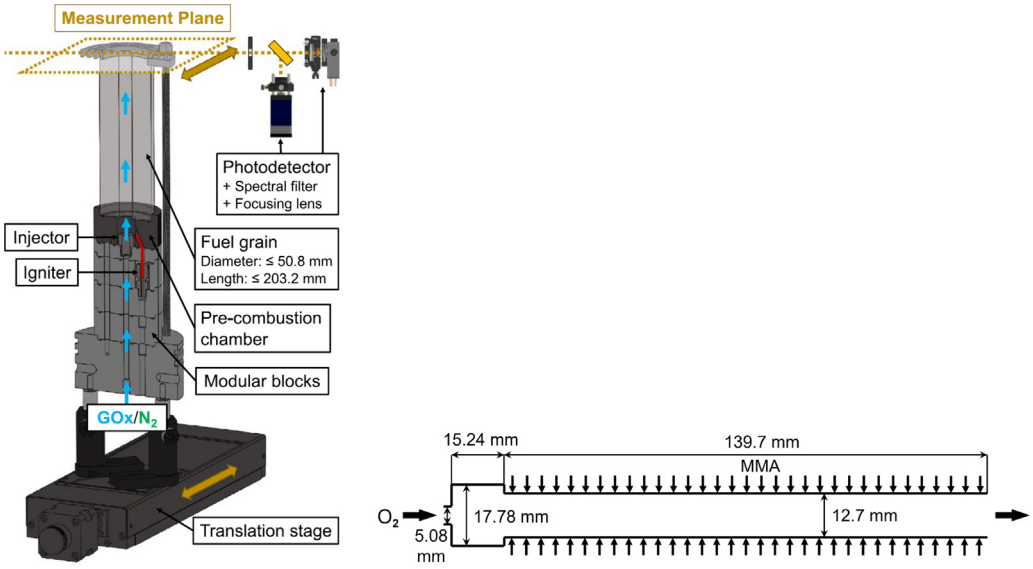

Fig. 2. Schematics of the experimental setup taken from Bendana et al. [15] (left) and the turbulent flow simulation setup (right).

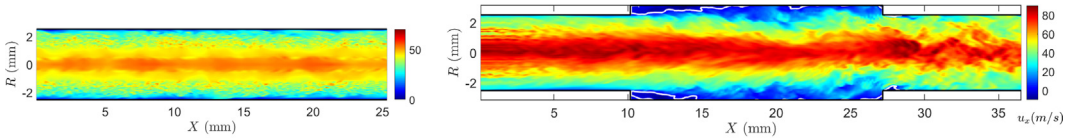

(a)Pipe flow with periodic boundary conditions (b)Injector with expansion chamber

Fig. 3. Axial velocity contours of a turbulent pipe flow with periodic boundary conditions in the axial direction (left). Axial velocity contours in an injector with an expansion chamber, with white lines corresponding to $u_x = 0$ (right).

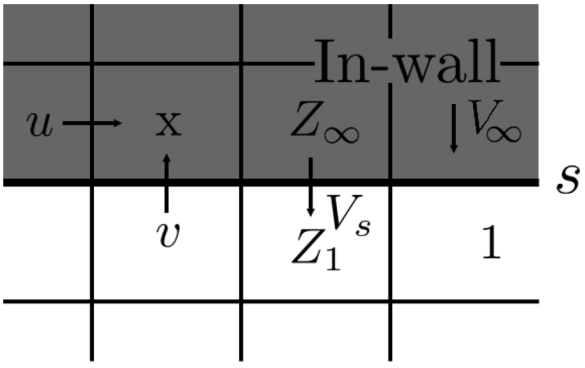

Fig. 4. Boundary conditions at the wall.

plotted in Fig. 3(b). The velocity information from the exit plane of the second simulation, as seen in Fig. 3(b), is used as the inlet for the combustion simulations.

2.4. Boundary conditions

The conversion (phase change) of solid PMMA into gaseous MMA at the wall is a complex physico-chemical process. In the present work, it is treated as a phase change and requires special consideration of the wall boundary conditions in NGA. Specifically, the solid PMMA is treated as a wall with outflow. No-slip boundary conditions are implemented at the wall, and the non-zero wall-normal velocity is calculated in real-time to account for the injection of gaseous MMA into the boundary layer (Fig. 4).

For computational consistency within the NGA framework, the PMMA velocity deep inside the fuel port is given by V_∞, and the MMA velocity at the wall surface is given by V_s. The mass flux, m'', is given by

$$m'' = \rho_\infty V_\infty = \rho_s V_s, \tag{8}$$

where ρ_∞ and ρ_s are the density of PMMA inside the wall and gaseous MMA at the wall surface, respectively. For a given passive scalar, Z, the scalar flux is given by,

$$\rho_\infty V_\infty Z_\infty = \rho_s V_s Z_s - \rho_s \alpha \frac{\partial Z}{\partial n}\bigg|_s, \tag{9}$$

where $Z_\infty = 1$ is the value of the passive scalar inside the wall, Z_s is the value of the passive scalar at the wall surface, and $\frac{\partial Z}{\partial n}|_s$ is the magnitude of the wall-normal gradient of the passive scalar at the wall surface.

For temperature, however, heat transfer to the wall needs to be included. It is assumed that all of the heat transferred into the solid wall is through conduction, calculated from $\frac{\partial T}{\partial n}|_s \neq 0$. This heat conduction to the wall dictates the rate of thermal decomposition of the solid PMMA and in turn the influx at the wall of gaseous MMA. In other words, the mass flux is related to the wall gradient of temperature by,

$$\rho_s V_s = \lambda \frac{\partial T}{\partial n}\bigg|_s / h_L, \tag{10}$$

where λ is the conductivity of gaseous MMA, and $h_L = 5.8 \times 10^5$ J/kg is the chosen effective heat of phase change of PMMA [38,39]. The wall surface temperature, T_s is taken as the approximate temperature at which PMMA undergoes its phase change, namely $T_s = 698\,K$. The pre-combustion chamber wall and the injector wall are modeled as isothermal walls at a temperature of 298 K, with no-slip boundary conditions.

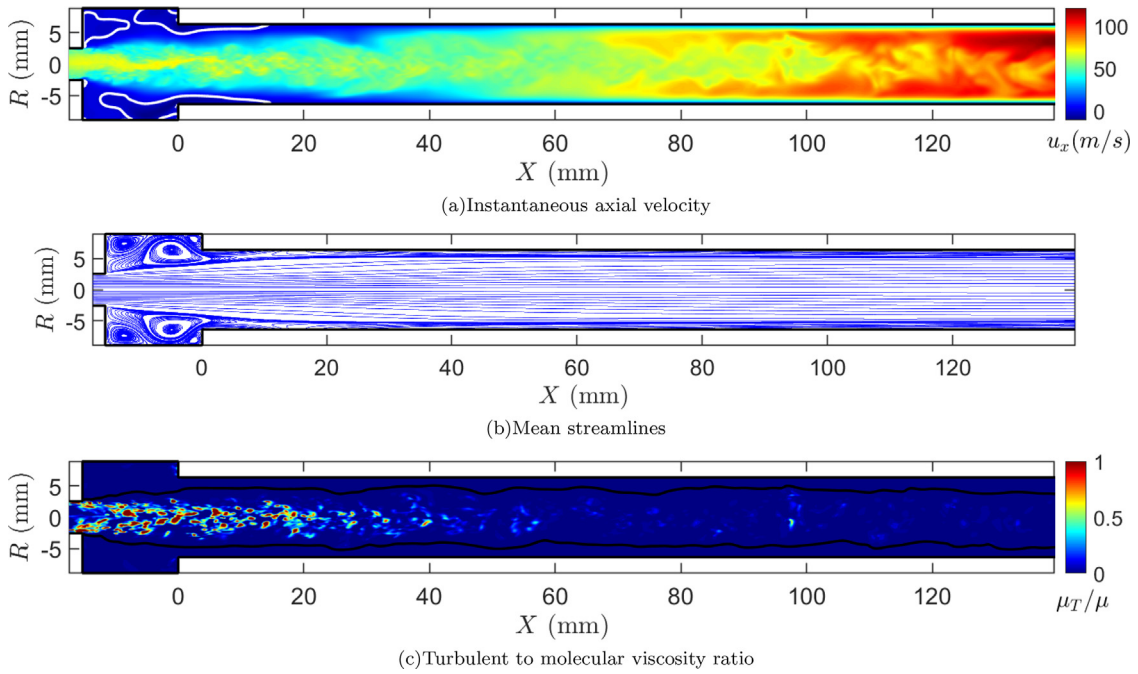

Fig. 5. Axial velocity contours (top) with white lines corresponding to $u_x = 0$. Streamlines from the mean velocity field, averaged over time and azimuthal angle, θ (middle). Ratio of turbulent viscosity to molecular viscosity (μ_T/μ) (bottom), with black lines corresponding to $Z_{st} = 0.3425$, where the mixture is stoichiometric. The results are from the mixture-averaged simulations, with non-unity Lewis numbers.

2.5. Initial conditions for the simulations

The simulation in the current study consists of flow in a cylindrical combustion chamber, with gaseous MMA introduced through the pipe walls, resulting in a turbulent diffusion flame.

Several simulations were performed with increasing levels of complexity to reduce the transient period and save computational resources. First, the fuel (gaseous MMA) was introduced into the domain uniformly through the walls of the pipe in addition to pure oxygen flowing through the injector, with no chemical reactions enabled between the two species. The results from the turbulent mixing simulation were used to initialize the unity Lewis number turbulent flame simulation. Diffusion flamelet values were used to estimate the temperature, density, and chemical composition throughout the domain, including combustion products from the mixture fraction and scalar dissipation rate. This allowed a realistic mixture state to be specified at every point in the domain, which served as the initial condition for simulations with full detailed chemistry. Once the unity Lewis number simulation reached a statistically stationary state, a snapshot from that simulation was in turn used to initialize the mixture-averaged case.

3. Simulation results

The results of the simulations are presented below, starting with a discussion of the flow field in Section 3.1. Section 3.2 presents an overview of the combustion processes and the two detailed chemistry flames are compared to observe the effects of differential diffusion in Section 3.3. The unity Lewis number simulation results are compared to one-dimensional diffusion flames in Section 3.4 and the same simulation is performed with a tabulated chemistry model, which is elaborated on in Section 3.5. The simulation results are compared to the experimental results in Section 3.6, and simulation results for a geometry with a larger fuel port diameter are provided later. All simulation results in the following sections are taken from the reacting simulations.

3.1. Flow field

The instantaneous axial velocity contours are plotted in Fig. 5(a), with the white lines corresponding to zero axial velocity. The locations at which these white lines meet the fuel surface highlight the re-attachment points of the flow, and also illustrate the re-circulation zones present in the combustion and pre-combustion chambers. This shows that a small amount of gaseous fuel is convected into the pre-combustion chamber. This is further corroborated by the streamlines extracted from the mean velocity field in Fig. 5(b). This re-circulation zone has been discussed and reported on in multiple works in the context of hybrid rockets [14,40,41], and it is known to have a significant effect on wall heat transfer [42]. As the flow moves further downstream, the temperature increases due to combustion processes occurring near the fuel port walls. This causes the density of the mixture to decrease as it travels downstream and consequently, the velocity increases as the flow moves downstream.

Contours of the ratio μ_T/μ are shown in Fig. 5(c). The value is zero where the effect of the LES model is insignificant and of order unity (with a maximum value of 5.7) where the LES model has a significant impact on the flow. It can be seen that the LES model is active mostly within the shear layer generated by the oxidizer jet entering the combustion chamber, where maximum values of about 5–6 were found. For the majority of the combustion chamber, especially in the reacting regions near the wall, μ_T/μ is much less than unity, which indicates that the effect of the LES model is negligible. In this region, the simulation is effectively a DNS (with no sub-grid scale model), as the high temperature of the mixture increases its molecular viscosity and reduces the Reynolds number significantly. This results in lower turbulence levels near the flames and the solid PMMA walls, which is why very little turbulent viscosity is included in these areas. The near wall y+ values ($y+ = u^\tau \Delta y|_w/\nu_w$) are in the range 0.2–0.6 in the injector pipe, 0–0.3 in the expansion chamber, and 0–0.6 in the combustion chamber, where $u^\tau = \sqrt{\tau_w/\rho}$ is the friction velocity, $\Delta y|_w$ is the near-wall grid spacing in the radial direction and ν_w is the kinematic

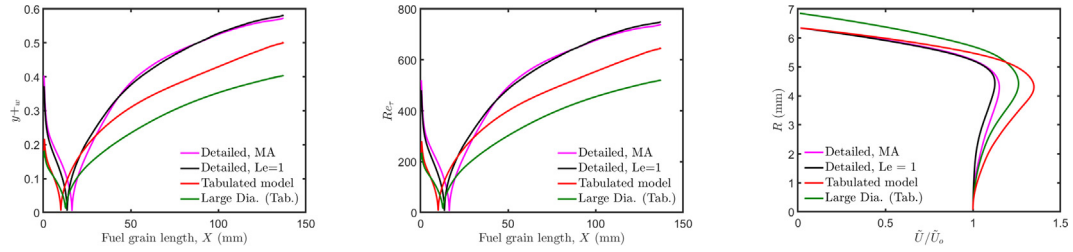

(a)$y+$ (b)Wall Reynolds number (c)Mean velocity (X = 139.7 mm)

Fig. 6. $y+$ (left) and Reynolds number at wall (middle) against fuel grain length. Mean velocity profile against radius at X = 139.7 mm (right), normalized by the mean centerline velocity. The magenta, black, red, and green lines correspond to the temporal and azimuthal averages from the mixture-averaged detailed, unity Lewis number detailed, tabulated, and large diameter cases respectively. (For interpretation of the references to colour in this figure legend, the reader is referred to the web version of this article.)

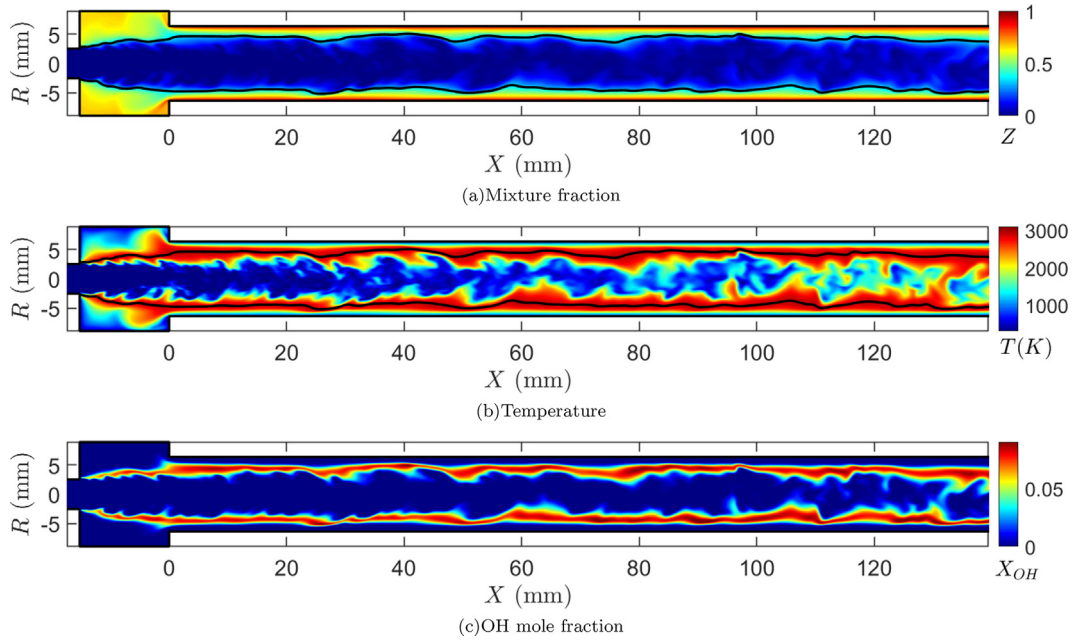

(a)Mixture fraction (b)Temperature (c)OH mole fraction

Fig. 7. Instantaneous contours of mixture fraction (top), temperature (middle), and OH mole fraction (bottom) from the mixture-averaged simulations. Black lines correspond to $Z_{st} = 0.3425$, where the mixture is stoichiometric.

viscosity at the wall. The y+ values in the combustion chamber in particular are plotted in Fig. 6(a) and the wall Reynolds number, $Re_\tau = R_w u^\tau / \nu_w$, where $R_w = 6.35$ mm is the initial combustion chamber radius, are plotted in Fig. 6(b). These values are low for all four simulations, suggesting the flow is laminar near the combustion chamber walls. Hence there is no need for wall modelling in these simulations. The simulations can be characterized as a hybrid DNS-LES, with sub grid scale models employed in the shear layer, generated by the injector flow. The normalized mean axial velocity profiles at X = 139.7 mm are plotted in Fig. 6(c). The maximum velocity is not achieved at the center, but instead 2 mm away from the wall, at the flame location where the density is lowest.

The oxygen mass flow rate is 1.2 g/s. The overall mass flow rate increases downstream in the combustion chamber as more fuel is being injected and is 1.7-1.9 g/s near the exit, with little variation between cases. The Reynolds number at the injector is $Re_{fig3}(a) = R_{fig3}(a) U_{o,inj} / \nu_{O_2,\,298\,K} = 46000$, where $R_{fig3}(a) = 2.54$ mm is the radius of the injector and $U_{o,inj}$ is the mean velocity at the injector. The Reynolds number calculated using the mean axial velocity increases from 1300 to 2300 going downstream in the combustion chamber if using the viscosity at the flame, $Re_f = R_w \overline{U}(x) / \nu_f(x)$, and decreases from 8000 to 2000 if using the viscosity at the axis, $Re_0 = R_w \overline{U}(x) / \nu_{R=0}(x)$, where $\overline{U}(x)$ is the mean axial velocity at axial location x and $\nu_f(x)$ is the viscosity at the flame at axial location x.

3.2. Overview of reacting fields

A snapshot of the contours of the mixture fraction, Z, is shown in Fig. 7(a). As expected, fuel-rich mixtures are found along the sides of the solid PMMA walls where the fuel is injected. A significant amount of the fuel-rich mixture is being convected into the pre-combustion chamber.

A snapshot of the temperature contours after the initial transient period is plotted in Fig. 7(b). The flame surface is highly wrinkled, as turbulence has developed in most of the region, owing to the high speeds and the three-dimensional resolution of the computational domain. The mole fraction of the hydroxyl radical, OH, is shown in Fig. 7(c), which gives an indication of the location of the flame. The maximum value of X_{OH} is around 0.092. The flame is anchored near the oxygen inlet at the edge where the injector meets the pre-combustion chamber, and the flame gets more wrinkled as the flow goes further downstream.

The presence of fuel where the oxygen is being injected anchors the flame at the inlet. This flame anchoring location is due to the method in which this simulation was initialized - by

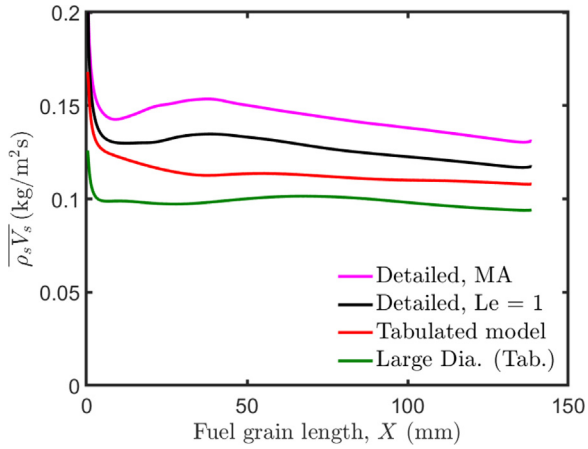

Fig. 8. Mean fuel inlet mass flux at the wall. The magenta, black, red and green curves correspond to the temporal and azimuthal averages from the mixture-averaged detailed, unity Lewis number detailed, tabulated, and large diameter cases respectively. (For interpretation of the references to colour in this figure legend, the reader is referred to the web version of this article.)

creating an initial condition based on a simulation with mixing only (no chemical reactions), unburnt fuel is able to accumulate in the pre-combustion chamber. The flame stabilizes along the shear layer in the pre-combustion chamber, which is a result of the axial injector and pre-combustion chamber geometry used in this study (Figs. 5 and 7). The existence of a shear layer and re-circulation zone is a commonly observed phenomena for similar axial injector configurations, and is documented in both the hybrid rocket and solid fuel ramjet studies [41,43,44]. The stabilization of the flame in the shear layer has been previously observed in an experimental setup with a similar geometry [44].

The time-averaged fuel injection mass flux at the PMMA surface is plotted as a function of the axial distance, x, in Fig. 8. The wall-normal mass flux is zero throughout the pre-combustion chamber. A large mass flux is observed near the leading edge of the combustion chamber ($x = 0$), where the flame is closest to the wall and the temperature gradients are the largest. From a practical point of view, this would translate to a fast erosion of the corner and a smoother edge (this effect is not included in the simulations). A local maximum of the wall mass flux occurs around 35 mm in the detailed chemistry cases, which is consistent with the regression rate profiles measured from experiments by Mechentel [13] and the theory discussed in [42]. In the tabulated cases, this local maximum is less pronounced, and moves downstream for the combustion chamber with larger internal diameter.

3.3. Effects of differential diffusion

Figure 13 shows the mean radial profiles of mole fractions of the combustion products, H_2O, CO_2, and CO, averaged over time and azimuthal angle, θ, at two different axial locations, 38.1 mm and 139.7 mm. As mentioned earlier, the experimental results were obtained at a distance of 0.5 mm downstream of the exit plane of the two different fuel grain lengths. The simulation results are calculated at the corresponding axial locations inside the combustion chamber for the detailed and tabulated cases. Functionally, the profile shapes extracted from the simulations are very close to the ones from the experiments, with small quantitative differences between them. There are few differences due to differential diffusion in the flow field (see Fig. 6). However, the mixture-averaged simulation shows 10–12% higher fuel mass flux compared to the unity Lewis number case. This is due to the higher density observed near the combustion chamber wall because of differential diffusion. Figure 9 shows the mean radial profiles of mole fractions of the combustion products, H_2O, CO_2, and CO, averaged over time and azimuthal angle, θ, at two different axial locations, 38.1 mm and 139.7 mm. As mentioned earlier, the experimental results were obtained at a distance of 0.5 mm downstream of the exit plane of the two different fuel grain lengths. The simulation results are calculated at the corresponding axial locations inside the combustion chamber for the mixture-averaged and unity Lewis number detailed cases.

The mole fraction profiles from the simulations and experiments exhibit similar trends. For the short fuel port (i.e. 38.1 mm), the two simulations exhibit equivalent profiles with a peak value of 0.25 for H_2O, 0.20 for CO_2. For the H_2O and CO_2 mole fractions at the longer fuel port (i.e. 139.7 mm) location, the mixture-averaged simulation results agree better with the experiments, and the unity Lewis number simulations slightly under-predict the peak values. For CO, regardless of fuel port length and diffusion modeling, both simulations predict peak values around 0.45, whereas the experiments report values around 0.3 and 0.35 for the two fuel port lengths.

The locations of the peak values also show minor differences between the three results. The peak locations of H_2O from the simulations and experiments are very close to each other. The two simulations are slightly removed from each other for CO_2, while the mixture-averaged diffusion simulations show better agreement with experiments. The peak locations of the CO profiles from the simulations are close to each other, but in comparison to the experiments, shifted to a smaller radius for the short fuel port and are about right for the longer fuel port. Overall, the radial profiles from the mixture-averaged simulations agree about the same or better with experimental results, when compared to those from the unity Lewis number simulations.

3.4. Comparison to one-dimensional flames

The results from the unity Lewis number 3D simulations are compared with those from 1D counterflow diffusion flame simulations using FlameMaster [45], across 200 grid points. The 1D counterflow diffusion flames consist of an oxidizer stream with the boundary conditions, $Z_{O_2} = 0$, $X_{O_2} = 1$, $T_{O_2} = 298\,K$, and a fuel stream with the boundary conditions, $Z_F = 1$, $X_F = 1$, $T_F = T_s - h_L/c_p = 427\,K$, at a pressure of 1 atm, where c_p is the heat capacity of gaseous MMA, with unity Lewis numbers for direct comparison with the turbulent case simulations. The mixture is calculated to be at stoichiometry at a value of $Z_{st} = 0.3425$. Inspired by droplet evaporation and combustion [46], the lower temperature of the fuel stream accounts for the heat loss at the wall due to the endothermic decomposition of the solid PMMA, instead of simply using the wall temperature from the 3D simulations, 698 K. The inset in Fig. 10(a) shows that near wall values of temperatures and mixture fractions from the detailed chemistry can be approximated into a linear fit, which can be extrapolated to $T_F = 427\,K$ at $Z_F = 1$, thus confirming the pure fuel stream temperature. A defining characteristic of these counterflow diffusion flames is the scalar dissipation rate, $\chi = 2\alpha|\nabla Z|^2$.

As seen in Fig. 10(a), the temperature values from the 3D simulation plateau around a maximum value of 3000 K for mixture fraction values between 0.2 and 0.5, around the stoichiometric value, 0.3425. The thick 1D flame ($\chi_{st} = 10\,s^{-1}$) exhibits a similar temperature plateau as in the 3D simulation, whereas the thin 1D flame ($\chi_{st} = 4000\,s^{-1}$) reaches a peak temperature of 3000 K at $Z = 0.45$. Interestingly, the scatter in the 3D data is mostly contained between the values from the two extreme cases of 1D diffusion flames. There was little difference between the graphs plotted for different locations, hence a consolidated single graph is provided in Fig. 10.

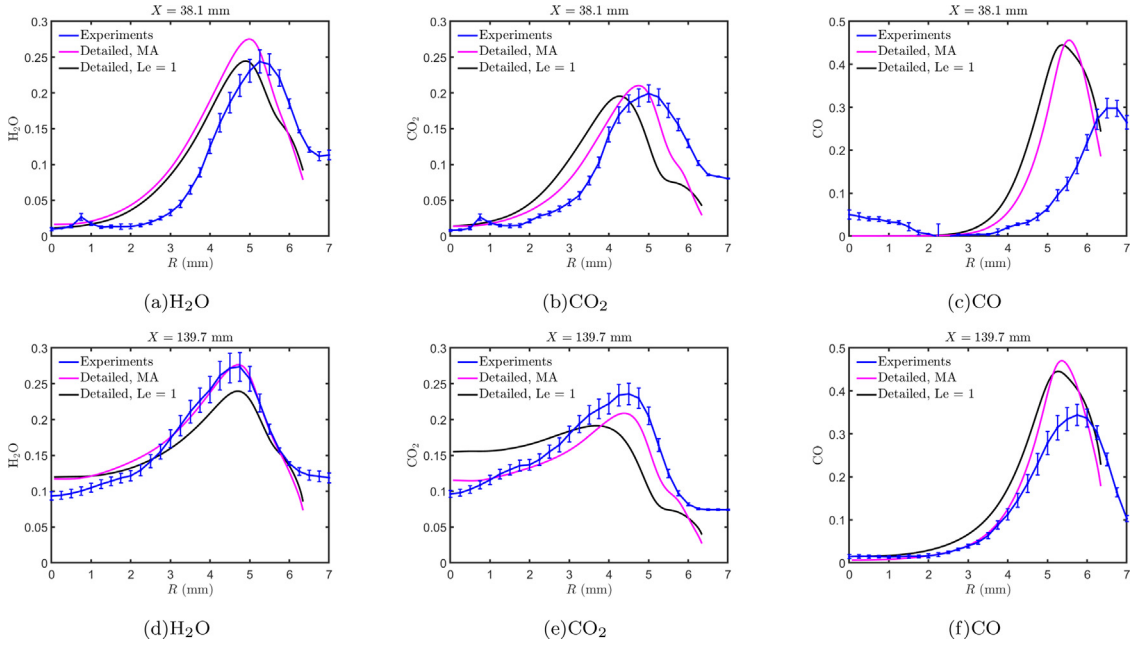

Fig. 9. Mean radial profiles of H_2O (left), CO_2 (middle), and CO (right) mole fractions at 38.1 mm (top) and 139.7 mm (bottom). The magenta and black curves correspond to the averages from the mixture-averaged detailed and unity Lewis number detailed cases, respectively. The blue symbols correspond to the experimental results from Bendana et al. [15]. (For interpretation of the references to colour in this figure legend, the reader is referred to the web version of this article.)

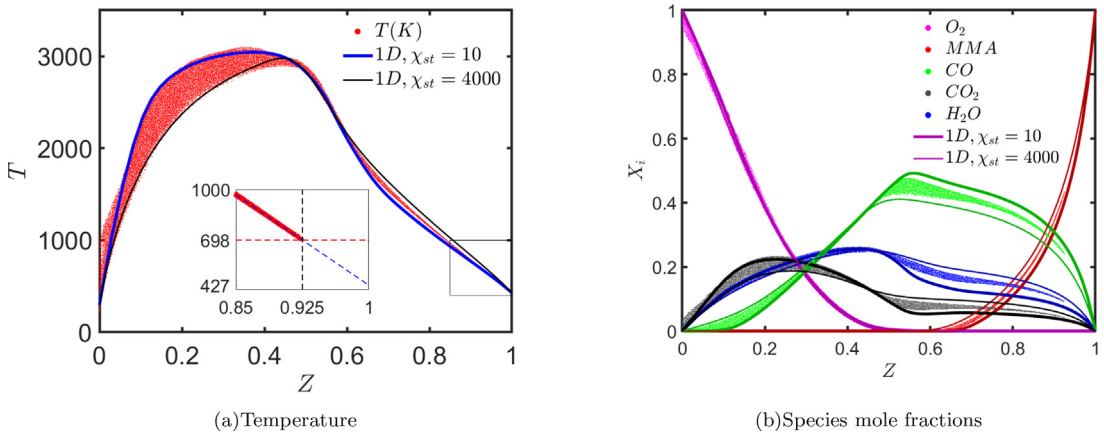

Fig. 10. Scatter plots of unity Lewis number simulation quantities against mixture fraction, and comparison with 1D simulation quantities. The thick lines correspond to $\chi_{st} = 10\,s^{-1}$ and the thin lines correspond to $\chi_{st} = 4000\,s^{-1}$. In the inset (left), the blue dashed line corresponds to a linear fit based on the near-wall values; the red dashed line corresponds to the wall temperature of $T_s = 698\,K$; and black dashed line corresponds to the average mixture fraction at the wall $Z_s = 0.925$. (For interpretation of the references to colour in this figure legend, the reader is referred to the web version of this article.)

A similar comparison is performed for the reactants' and products' mole fractions in Fig. 10(b). Once again, the instantaneous values are enveloped by those from the two extreme cases of 1D diffusion flames. The most spread is seen in the carbon monoxide mole fraction, in the 3D simulations as in the two 1D diffusion flames. Most of the chemistry is comparable to 1D diffusion flames and is captured by the range of χ_{st} considered. χ_{st} reaches a maximum value of 3600 in the detailed chemistry simulations and is significantly below the scalar dissipation rate at extinction, $\chi_{st} =$ 46400, obtained from 1D diffusion calculations.

3.5. Tabulated chemistry

The 1D counterflow flame simulation results are used to perform additional simulations with tabulated chemistry, as the temperature and species mole fractions from these 1D simulations compare well with the 3D simulation results using finite rate chemistry and unity Lewis number. In these simulations, the only scalar transported is the mixture fraction, Z. The required variables like temperature and mole fraction of the species are computed from the mixture fraction and scalar dissipation rate, namely $T = T(Z, \chi)$ and $Y_i = Y_i(Z, \chi)$. Practically, this functional dependence was obtained by tabulating the results of 24 different 1D counterflow diffusion flames, over a wide range of χ_{st} ($2 \times 10^{-2}\,s^{-1}$ to $2 \times 10^{4}\,s^{-1}$), simulated using FlameMaster. The same chemical kinetics model and transport properties were used in the flamelet solver as in the detailed chemistry NGA simulations.

Since the temperature is not solved for directly in the tabulated chemistry simulation, Eq. (10) cannot be used anymore, and the mass flux at the wall is calculated now from Eq. (9) as

$$\rho_s V_s = -\rho_s \alpha \left.\frac{\partial Z}{\partial n}\right|_s / (1 - Z_s), \tag{11}$$

where Z_s is the mixture fraction corresponding to the temperature of the gas next to the fuel wall, $T_s = 698\,K$. It is important to highlight that Z_s is not unity, as a direct consequence of

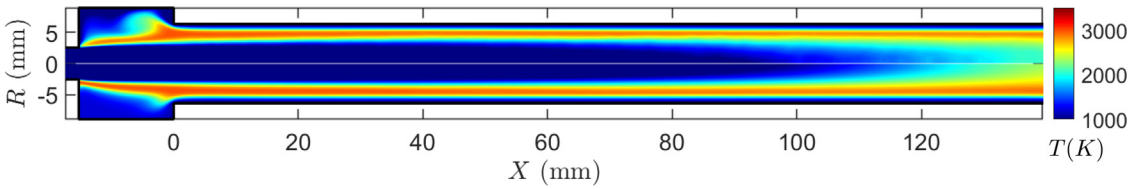

Fig. 11. Time-averaged and rotationally averaged temperature contours, from unity Lewis number detailed chemistry (top) and tabulated chemistry (bottom) simulations.

the boundary condition used (Eq. (9)). While this quantity may be calculated in real-time, the current simulations use a constant value of $Z_s = 0.925$ for numerical stability. This value was obtained by extrapolating values within the computational domain to the wall using instantaneous results of detailed chemistry simulations, as $Z_s = 0.9251 \pm 0.0006$ (using the linear fit in Fig 10(a)). There are two strategies for solving the flamelet equations: either use $T(Z_s) = T_s = 698\,K$ as the boundary condition, or use $T(Z_F = 1) = T_s - h_L/c_p = 427\,K$. The second one was preferred in the present work for stability. That being said, the thermal diffusivity, α, and density, ρ_s, are extrapolated in real-time. The authors also tried to calculate the fuel inflow rate from Eq. (10), with the estimated temperature, $T = T(Z, \chi)$. This proved to be unstable as $\chi = 2D|\nabla Z|^2$ includes D, which is calculated as $D(Z, \chi)$. There was little difference between the fuel inflow calculated using the two different methods.

The time-averaged and rotationally averaged temperature contours from the unity Lewis number detailed chemistry and tabulated chemistry simulations are plotted in Fig. 11. The results are qualitatively and quantitatively similar. The figure shows the average over long periods of time, which is influenced by the flame front moving radially in the two different cases. This instability was found to be highly sensitive to the global equivalence ratio, as we go further downstream, which explains the differences in the downstream portions of the combustion chamber. As expected, the tabulated chemistry simulation is more efficient, computationally. When using 156 Intel Xeon X5650 processors with InfiniBand QDR interconnect, the computational time per iteration, per grid point, is 2400 μs for detailed chemistry simulations and 115 μs for tabulated chemistry simulations. The detailed simulations utilized 375,000 CPU hours, whereas the tabulated simulations only used 18,000 CPU hours. The principal reason for the cost savings is the reduction of the number of transported scalars from 88 (for finite rate chemistry) to 1 (for tabulated chemistry). Both simulations were performed with 4 sub-iterations per time step.

3.6. Comparison with experiments

As discussed previously, the experiments were performed with ten different experimental configurations with fuel grain lengths of 12.7 mm (0.5 in.) intervals. In the experiments, the fuel injection rate was estimated by using the mass difference in the fuel port and the burn time. This fuel injection rate was in turn used to estimate a mean diameter at the middle of the burn time and consequently the mean internal surface area. In the simulations, the fuel regression rate is calculated from the fuel injection mass flux using the relation

$$\dot{r} = |\rho_s V_s|/\rho_\infty \tag{12}$$

where $\rho_\infty = 1185\,kg/m^3$ is the density of solid PMMA at room temperature [47]. The fuel regression rate is averaged over different port lengths, and is plotted against the fuel grain length for the detailed and tabulated simulations in Fig. 12(a).

The fuel regression rate calculated from the experiments decreases with increasing fuel grain length, with a few exceptions. In the simulations, there is very little dependence on the fuel grain length, and the values are within the range of experimental values of regression rate. Interestingly, the results obtained with unity Lewis number yield a slightly lower regression rate compared to those obtained with mixture-averaged diffusion (about 12%) and the tabulated chemistry predicts an even lower regression rate compared to those obtained with detailed finite rate chemistry. It should be noted that the shorter fuel grain experiments compare better with the detailed chemistry simulations and the longer grain experimental results lie closer to the tabulated simulation results.

The fuel mass flow rates are calculated by integrating the inflow mass flux through the internal walls of the combustion chamber. The global oxidizer to fuel ratio by mass, O/F, is calculated from both simulations and the experiments and is plotted against the fuel grain lengths in Fig. 12(b). It should be noted that the oxidizer mass flow rate is the same across all trials (namely $1.2 g/s$), and the fuel mass flow rate is proportional to the fuel grain length (since $\dot{r}$ is almost constant). As a result, the O/F ratio is inversely proportional to the fuel grain lengths, and there is good agreement between the experiments and simulations.

Figure 13 shows the mean radial profiles of mole fractions of the combustion products, H_2O, CO_2, and CO, averaged over time and azimuthal angle, θ, at two different axial locations, 38.1 mm and 139.7 mm. The simulation results are calculated for the unity Lewis number detailed and tabulated cases, at axial locations inside the combustion chamber corresponding to the different fuel lengths in the experiments.

The H_2O and CO_2 mole fraction profiles exhibit similar trends. For the short fuel port (i.e. 38.1 mm), the simulations and experiments exhibit similar profiles with a peak value of 0.25 for H_2O and 0.20 for CO_2. However, the locations of the peak values from the simulations are about 1 mm away from those of the experiments. For the larger fuel port (i.e. 139.7 mm), the simulations slightly under-predict the peak values of H_2O and CO_2 mole fractions, while the peak locations are very close to each other.

The major difference between the experimental and simulation results is in the CO mole fraction shown in Fig. 13(c) and (f). Consistent with the H_2O and CO_2 results, the peak locations of the CO profiles from the simulations are shifted to a smaller radius for the short fuel port and are about right for the longer fuel port. There is, however, disagreement on the peak CO values between the simulations and experiments. Regardless of fuel port length and chemistry modeling, the simulations predict peak values around 0.45, whereas the experiments report values around 0.3 and 0.35 for the two fuel port lengths. It is uncommon in simulations to capture the profiles of two of the three major products (H_2O and CO_2) and not that of the third one (CO). An analysis of the 1D counterflow results indicated that peak values less than 0.4 could not be reached even with extreme scalar dissipation rates (see Fig. 10). The same analysis showed that four species make up most of the mole fraction at these locations: CO, H_2O, CO_2, and MMA. Such a discrepancy only in the CO profile would imply a similar discrepancy in the MMA mole fraction, which in turn would likely change the entire flow field. This discrepancy is still an open topic of investigation.

One possible explanation the authors considered is a lack of spatial resolution to capture the reaction zone. The maximum

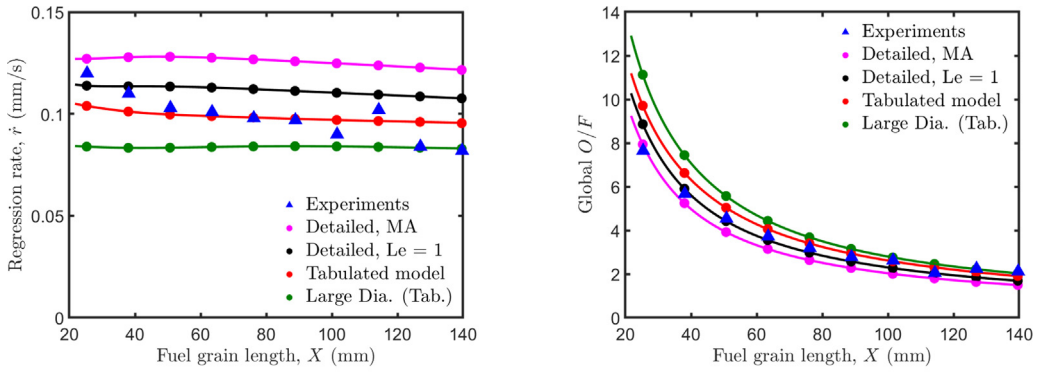

(a)Mean fuel regression rate (b)Global oxidizer to fuel ratio

Fig. 12. Mean fuel regression rate (left) and global oxidizer to fuel ratio (right) against fuel grain length. The magenta, black, red, and green circles correspond to the temporal and azimuthal averages from the mixture-averaged detailed, unity Lewis number detailed, tabulated, and large diameter cases respectively. The blue triangles correspond to experimental results from Bendana et al. [15]. (For interpretation of the references to colour in this figure legend, the reader is referred to the web version of this article.)

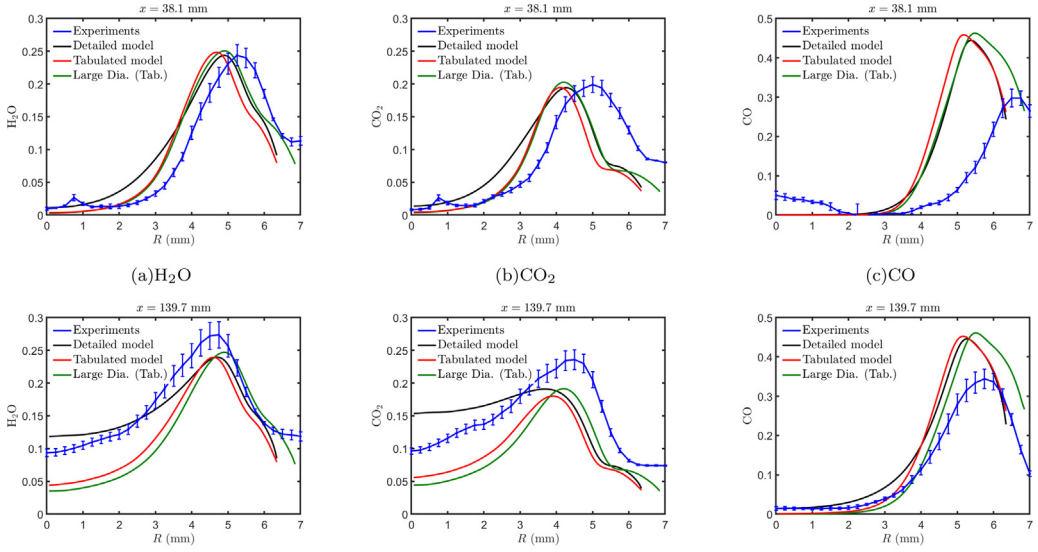

(a)H_2O (b)CO_2 (c)CO

(d)H_2O (e)CO_2 (f)CO

Fig. 13. Mean radial profiles of H_2O (left), CO_2 (middle), and CO (right) mole fractions at 38.1 mm (top) and 139.7 mm (bottom). The black, red, and green curves correspond to the averages from the unity Lewis number detailed, tabulated, and large diameter cases, respectively. The blue symbols correspond to the experimental results from Bendana et al. [15]. (For interpretation of the references to colour in this figure legend, the reader is referred to the web version of this article.)

value of scalar dissipation rate at the flame location was calculated to be $\chi_{st} = 3600$ in the combustion chamber, which corresponds to a minimum flame thickness of $l_f = 2Z_{st}/|\nabla Z| = 0.92$ mm. The grid spacing in the radial direction at the flame location is 0.063 mm, which is about 15 times smaller than the lowest flame thickness, enough to fully resolve the reactive zone. As mentioned earlier, the figures show the average over long periods of time, which is influenced by the flame front moving radially. This instability was found to be highly sensitive to the global equivalence ratio, as we go further downstream, which explains the differences between the simulations in the downstream portions of the combustion chamber, especially near the centerline.

Impact of changing fuel port diameter

The results from the large-diameter simulations are also included in the comparison to the experimental results in Figs. 6, 8, 12, and 13. The oxygen inflow rate remains the same in this simulation (1.2 g/s) and the overall fuel mass inflow rate remains fairly similar across the four cases. The larger surface area in the wider fuel port simulations leads to a smaller fuel inlet velocity. This in turn decreases the regression rate of the solid fuel and has only limited impact on the global O/F ratio. The change did not affect the peak value of the mole fraction profiles and the peak locations moved a small distance away from the axis.

4. Conclusions

Combustion studies of MMA/GO_x were performed using finite-rate detailed chemistry hybrid DNS-LES, in 3D combustion chamber setups, with wall inflow. Boundary conditions were developed for a wall with fuel inflow while accounting for heat conduction and temperature-dependent fuel inflow at the wall. The computational setup is used to simulate turbulent flames involving MMA and oxygen, and the simulations are stable in time. A local maximum of fuel regression rate is predicted in the vicinity of the jet re-attachment point, which is consistent with experiments. The flow field and reacting conditions were analyzed to locate and observe regions in the computational domain, where different physical and chemical phenomena dominate and/or interact.

The mixture-averaged Lewis number and unity Lewis number simulations were compared to observe the differential diffu-

sion effects. The temperature and mole fraction profiles from the unity Lewis number 3D simulations are comparable to 1D diffusion flames, under similar thermodynamic conditions. Tabulated chemistry models were developed and used to improve the computational efficiency of the simulations. Tabulated chemistry simulations were performed on a combustion chamber with a larger internal diameter. The tabulated simulations were contrasted with the unity Lewis number case to understand the chemistry effects, while the geometric effects were analyzed by comparing the two tabulated chemistry simulations.

While the mixture-averaged Lewis number and unity Lewis number simulations showed similar flow field profiles, there were significant changes in the mole fraction profiles, fuel mass flux, and subsequently the fuel regression rate, due to differential diffusion effects. The tabulated chemistry simulations had different flow field profiles and regression rates, while the radial profiles of H_2O, CO_2, and CO were similar to the unity Lewis number simulations in peak values and locations. The two tabulated simulations showed slight differences which are consistent with the change in the internal radius of the combustion chamber.

If one wishes to capture the flow field profiles and fuel regression rate, chemistry effects are important. If one wishes to capture the internal chemistry profiles of the combustion products, differential diffusion effects need to be included. The wall regression rates from all the simulations fall within the range of the experimental values and the radial chemistry profiles from the mixture-averaged simulations agree fairly well with the experiments, showing the predictive capabilities of the simulations presented in this work.

Declaration of Competing Interest

The authors declare that they have no known competing financial interests or personal relationships that could have appeared to influence the work reported in this paper.

Acknowledgments

Parts of this work were performed at the Jet Propulsion Laboratory, California Institute of Technology, under a contract with the National Aeronautics and Space Administration. The authors would like to acknowledge the support of the JPL/Caltech President's and Director's Research and Development Fund for sponsoring this research.

Appendix A. Local flame-normal grid resolution for anisotropic grid

As mentioned in Section 2.2, the grid resolution is uniform in the axial direction (250 μm), with a stretched grid spacing in the radial direction, with the radial resolution being 10 μm near the wall. In an idealized case, the flame front would be parallel to the wall, hence one could surmise that the grid resolution in the radial direction is the most important to capture the chemistry effects. The grid spacing in the radial direction at the flame location is 0.063 mm, which is about 15 times smaller than the lowest flame thickness, 0.92 mm.

However, due to the turbulent nature of the flow, the flame front is not always parallel to the wall. The direction perpendicular to the flame front can be calculated as the direction of the gradient of the mixture fraction. Using this direction, an estimate of a local grid resolution perpendicular to the flame is calculated as

$$\Delta x_{f,\perp} = \frac{\nabla \mathbf{Z}}{|\nabla Z|} \cdot \left(\Delta x\, \mathbf{e_x} + \Delta r\, \mathbf{e_r} + r\Delta\theta\, \mathbf{e}_\theta\right).$$

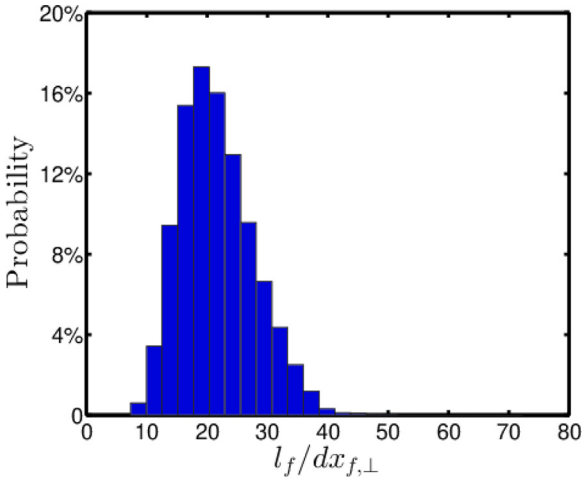

Fig. A.1. The probability distribution of the ratio of flame thickness to the local grid resolution perpendicular to the flame.

The median of the local grid resolution, $\Delta x_{f,\perp}$, was 0.12 mm, and based on the Δx 0.254 mm and Δr values mentioned above, the flame front is on average at a 13° angle to the wall. The flame thickness (l_f) ranges from 0.92 mm to 190 mm (estimated from the χ_{st} values in the turbulent simulations), with the median flame thickness around 2.52 mm. The distribution of the ratio of the flame thickness to the local grid resolution perpendicular to the flame is plotted in Fig. A.1.

The median ratio of flame thickness to the local grid resolution is around 21. Less than 1% of the regions are where the flame thickness is less than 10 times that of the grid resolution, hence the grid resolution is sufficient for 99% of the region.

References

[1] A. Conte, J. Rabinovitch, E. Jens, A. Chandler Karp, B. Nakazono, D. Vaughan, Design, modeling and testing of a O_2/CH_4 igniter for a hybrid rocket motor, Fluid Dynamics Conference (2018), p. 3239.
[2] D.M. Dyrda, F.S. Mechentel, B.J. Cantwell, A.C. Karp, J. Rabinovitch, E.T. Jens, Diode laser ignition of a poly (methyl methacrylate) and gaseous oxygen hybrid motor, J. Propul. Power 36 (5) (2020) 773–782.
[3] G.A. Marxman, C.E. Wooldridge, R.J. Muzzy, Fundamentals of hybrid boundary-layer combustion, Progr. Astronaut. Rocketry 15 (1964) 485–522.
[4] S. Yuasa, O. Shimada, T. Imamura, T. Tamura, K. Yamoto, A technique for improving the performance of hybrid rocket engines, 35th Joint Propulsion Conference and Exhibit (1999), p. 2322.
[5] T. Takashi, S. Yuasa, K. Yamamoto, Effects of swirling oxidizer flow on fuel regression rate of hybrid rockets, 35th Joint Propulsion Conference and Exhibit (1999), p. 2323.
[6] B. Greiner, R. Frederick Jr., Results of labscale hybrid rocket motor investigation, 28th Joint Propulsion Conference and Exhibit (1992), p. 3301.
[7] M. Masugi, T. Ide, T. Sakurai, S. Yuasa, N. Shiraishi, T. Shimada, Visualization of flames in combustion chamber of swirling-oxidizer-flow-type hybrid rocket engines, 46th AIAA/ASME/SAE/ASEE Joint Propulsion Conference & Exhibit (2010), p. 6546.
[8] C.J. Mady, P.J. Hickey, D.W. Netzer, Combustion behavior of solid-fuel ramjets, J. Spacecraft Rockets 15 (3) (1978) 131–132.
[9] P.A.O.G. Korting, C.W.M. van der Geld, T. Wijchers, H.F.R. Schoyer, Combustion of polymethylmethacrylate in a solid fuel ramjet, J. Propul. Power 6 (3) (1990) 263–270.
[10] E.T. Jens, A.C. Karp, J. Rabinovitch, A. Conte, B. Nakazono, D.A. Vaughan, Design of interplanetary hybrid cubesat and smallsat propulsion systems, 2018 Joint Propulsion Conference (2018), p. 4668.
[11] E.T. Jens, A.C. Karp, B. Nakazono, K.T. Williams, J. Rabinovitch, D. Dyrda, F.S. Mechentel, Low pressure ignition testing of a hybrid smallsat motor, AIAA Propulsion and Energy 2019 Forum (2019), p. 4009.
[12] G. Zilliac, G.T. Story, A.C. Karp, E.T. Jens, G. Wittinghill, Combustion efficiency in single port hybrid rocket engines, AIAA Propulsion and Energy 2020 Forum (2020), p. 3746.
[13] F.S. Mechentel, B.R. Hord, B.J. Cantwell, Optically resolved fuel regression of a clear polymethylmethacrylate hybrid rocket motor, J. Propul. Power 36 (5) (2020) 763–772.
[14] S. Mechentel, Preliminary design of a hybrid motor for small-satellite propulsion, Stanford University, 2019 PhD thesis.

[15] F.A. Bendana, I.C. Sanders, J.J. Castillo, C.G. Hagström, D.I. Pineda, R.M. Spearrin, In-situ thermochemical analysis of hybrid rocket fuel oxidation via laser absorption tomography of CO, CO_2, and H_2O, Exp. Fluids 61 (9) (2020) 1–13.
[16] G.D. Di Martino, C. Carmicino, R. Savino, Transient computational thermofluid-dynamic simulation of hybrid rocket internal ballistics, J. Propul. Power 33 (6) (2017) 1395–1409.
[17] D. Bianchi, B. Betti, F. Nasuti, C. Carmicino, Simulation of gaseous oxygen/hydroxyl-terminated polybutadiene hybrid rocket flowfields and comparison with experiments, J. Propul. Power 31 (3) (2015) 919–929.
[18] G. Leccese, D. Bianchi, F. Nasuti, Modeling and simulation of paraffin–based hybrid rocket internal ballistics, 2018 Joint Propulsion Conference (2018), p. 4533.
[19] C. Dennis, B. Bojko, On the combustion of heterogeneous AP/HTPB composite propellants: a review, Fuel 254 (2019) 115646.
[20] M.J. Chiaverini, K.K. Kuo, Fundamentals of hybrid rocket combustion and propulsion, American Institute of Aeronautics and Astronautics, 2007.
[21] H.R.R. Ranga, O.P. Korobeinichev, A. Harish, V. Raghavan, A. Kumar, I.E. Gerasimov, M.B. Gonchikzhapov, A.G. Tereshchenko, S.A. Trubachev, A.G. Shmakov, Investigation of the structure and spread rate of flames over PMMA slabs, Appl. Therm. Eng. 130 (2018) 477–491.
[22] A. Kacem, M. Mense, Y. Pizzo, G. Boyer, S. Suard, P. Boulet, G. Parent, B. Porterie, A fully coupled fluid/solid model for open air combustion of horizontally-oriented PMMA samples, Combust. Flame 170 (2016) 135–147.
[23] A. Rampazzo, F. Barato, Modeling and CFD simulation of regression rate in hybrid rocket motors, Fire 6 (3) (2023) 100.
[24] S. Dakshnamurthy, D.A. Knyazkov, A.M. Dmitriev, O.P. Korobeinichev, E.J.K. Nilsson, A.A. Konnov, K. Narayanaswamy, Experimental study and a short kinetic model for high-temperature oxidation of methyl methacrylate, Combust. Sci. Technol. 191 (10) (2019) 1789–1814.
[25] O. Desjardins, G. Blanquart, G. Balarac, H. Pitsch, High order conservative finite difference scheme for variable density low mach number turbulent flows, J. Comput. Phys. 227 (15) (2008) 7125–7159.
[26] B. Savard, Y. Xuan, B. Bobbitt, G. Blanquart, A computationally-efficient, semi-implicit, iterative method for the time-integration of reacting flows with stiff chemistry, J. Comput. Phys. 295 (2015) 740–769.
[27] M. Herrmann, G. Blanquart, V. Raman, Flux corrected finite volume scheme for preserving scalar boundedness in reacting large-eddy simulations, AIAA J. 44 (12) (2006) 2879.
[28] S. Lapointe, B. Savard, G. Blanquart, Differential diffusion effects, distributed burning, and local extinctions in high Karlovitz premixed flames, Combust. Flame 162 (9) (2015) 3341–3355.
[29] J.O. Hirschfelder, C.F. Curtiss, R.B. Bird, Molecular theory of gases and liquids, (1964).
[30] B. Savard, G. Blanquart, Broken reaction zone and differential diffusion effects in high Karlovitz n-C7H16 premixed turbulent flames, Combust. Flame 162 (5) (2015) 2020–2033.
[31] R.B. Bird, Transport phenomena, Appl. Mech. Rev. 55 (1) (2002) R1–R4.
[32] T.P. Coffee, J.M. Heimerl, Transport algorithms for premixed, laminar steady-state flames, Combust. Flame 43 (1981) 273–289.
[33] R.J. Kee, M.E. Coltrin, P. Glarborg, Chemically reacting flow: theory and practice, John Wiley & Sons, 2005.
[34] S. Mathur, P.K. Tondon, S.C. Saxena, Thermal conductivity of binary, ternary and quaternary mixtures of rare gases, Mol. Phys. 12 (6) (1967) 569–579.
[35] J.H. Ferziger, H.G. Kaper, Mathematical theory of transport processes in gases, Am. J. Phys. 41 (4) (1973) 601–603.
[36] M. Germano, U. Piomelli, P. Moin, W.H. Cabot, A dynamic subgrid-scale eddy viscosity model, Phys. Fluids A-Fluid 3 (7) (1991) 1760–1765.
[37] D.K. Lilly, A proposed modification of the Germano subgrid-scale closure method, Phys. Fluids A-Fluid 4 (3) (1992) 633–635.
[38] A.V. Singh, M.J. Gollner, A methodology for estimation of local heat fluxes in steady laminar boundary layer diffusion flames, Combust. Flame 162 (5) (2015) 2214–2230.
[39] J.P. de Wilde, Heat of gasification of polyethylene and polymethylmethacrylate, Memorandum Report, 1988.
[40] C. Carmicino, Acoustics, vortex shedding, and low-frequency dynamics interaction in an unstable hybrid rocket, J. Propul. Power 25 (6) (2009) 1322–1335.
[41] C. Carmicino, A.R. Sorge, Influence of a conical axial injector on hybrid rocket performance, J. Propul. Power 22 (5) (2006) 984–995.
[42] K.M. Krall, E.M. Sparrow, Turbulent heat transfer in the separated, reattached, and redevelopment regions of a circular tube, J. Heat Transf. 88 (1) (1966) 131–136.
[43] S. Krishnan, P. George, Solid fuel ramjet combustor design, Prog. Aerosp. Sci. 34 (3–4) (1998) 219–256.
[44] G. Schulte, R. Pein, A. Hogl, Temperature and concentration measurements in a solid fuel ramjet combustion chamber, J. Propul. Power 3 (2) (1987) 114–120.
[45] H. Pitsch, FlameMaster, a C++ computer program for 0D combustion and 1D laminar flame calculations (1998).
[46] M. Renksizbulut, M.C. Yuen, Experimental study of droplet evaporation in a high-temperature air stream, J. Heat Transf. 105 (2) (1983) 384–388.
[47] F. Yang, G.L. Nelson, PMMA/Silica nanocomposite studies: synthesis and properties, J. Appl. Polym. Sci. 91 (6) (2004) 3844–3850.